Quantifying species and age-dependent fibroblast morphologies on biomaterial surfaces via optical diffraction tomography

Biomaterials Advances 189 (2026) 215063

Contents lists available at ScienceDirect

Biomaterials Advances

journal homepage: www.journals.elsevier.com/materials-science-and-engineering-c

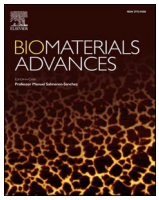

Quantifying species and age-dependent fibroblast morphologies on biomaterial surfaces via optical diffraction tomography

Francesco Formaggio [a,1], Pooja Anantha [b,1], Federica Trebbi [c], Vincenzo Palermo [d,e], Tamara Posati [d], Marianna Barbalinardo [f], Gioacchino Calandra Sebastianella [d], Simone Bonetti [f], Marco Caprini [a], Jessica Chen [g], Giovanna Sotgiu [d], Maira Bacchiega [h], Roberto Zamboni [d], Annalisa Convertino [i,**], Ishan Barman [b,j,k,**], Emanuela Saracino [d,*]

[a] Department of Pharmacy and Biotechnology, University of Bologna, via S. Donato 19/2, 40127, Bologna, Italy
[b] Department of Mechanical Engineering, Johns Hopkins University, Baltimore, MD, 21218, USA
[c] Department of Biomedical and Neuromotor Sciences, University of Bologna, Piazza di Porta S. Donato 2, 40126, Bologna, Italy
[d] Institute for Organic Synthesis and Photoreactivity, National Research Council, Via Gobetti 101, I-40129, Bologna, Italy
[e] Department of Industrial and Materials Science, Chalmers University of Technology, Gothenburg, Sweden
[f] Institute for the Study of Nanostructured Materials, National Research Council, Via Gobetti 101, 40129, Bologna, Italy
[g] Department of Biology, Johns Hopkins University, Baltimore, MD, 21218, USA
[h] Schaefer SEE Srl, Via Luigi Einaudi 23, 45100, Rovigo, Italy
[i] Institute for Microelectronics and Microsystems, National Research Council, via Fosso del Cavaliere 100, Rome, 00133, Italy
[j] Department of Oncology, Johns Hopkins University, Baltimore, MD, 21287, USA
[k] The Russell H. Morgan Department of Radiology and Radiological Science, Division of Cancer Imaging Research, Johns Hopkins University School of Medicine, Baltimore, MD, 21205, USA

ARTICLE INFO

Keywords:
Rodent and human fibroblasts
Morphology
Biomaterial surfaces
Optical diffraction tomography
Cell dry mass and area

ABSTRACT

Fibroblasts are essential for maintaining tissue structure by producing the extracellular matrix (ECM) and collagen fibers. Their potential in regenerative medicine and personalized therapy has recently attracted attention, particularly for reprogramming into neuronal cells. Despite ongoing methodological advances aimed at fully exploiting the potential of fibroblasts, variability in their responses, driven by donor-specific factors such as species and age, remains poorly understood.

In this study, we investigate fibroblasts differentiation in vitro, focusing on how biomaterial surfaces can guide cell growth, proliferation, and morphology through mechanical cues. We compare fibroblasts from two species (rodent and human) and, within the human donor group, across two distinct age ranges. By combining conventional morphological and cytoskeletal analyses with advanced three-dimensional (3D) label-free imaging techniques such as optical diffraction tomography (ODT), we characterize the morphological transformations of these cells cultured on two biomaterial surfaces, silk fibroin (SF) and Zinc-Aluminum hydrotalcite (HTlc), by measuring cell dry mass and projected area. Our findings provide insights into how substrate characteristics shape fibroblast morphology and introduce an effective strategy to identify substrates that preferentially promote neuron-like morphological shapes, an important feature for inducing neuronal reprogramming.

1. Introduction

Fibroblasts are connective tissue cells responsible for synthesizing the extracellular matrix (ECM) and collagen fibers [1], thereby providing structural support to tissues and organs. Owing to their abundance, accessibility, and high proliferative capacity, they have attracted considerable interest in regenerative medicine and personalized therapies. The limited regenerative capacity of the central nervous system (CNS) following injury or disease remains a major challenge. To overcome this limitation, direct reprogramming of fibroblasts into CNS-

* Correspondence to: E. Saracino, Institute for Organic Synthesis and Photoreactivity, National Research Council, Via Gobetti 101, 40129, Bologna, Italy.
** Corresponding authors.
E-mail addresses: annalisa.convertino@cnr.it (A. Convertino), ibarman@jhu.edu (I. Barman), emanuela.saracino@cnr.it (E. Saracino).
[1] These authors contributed equally.

https://doi.org/10.1016/j.bioadv.2026.215063
Received 16 March 2026; Received in revised form 29 June 2026; Accepted 11 July 2026
Available online 14 July 2026

specific neurons has emerged as a promising strategy for both cell replacement therapies and the development of physiologically relevant in vitro brain models [2–5]. This approach offers several advantages over traditional methods: i) reduced risks of cell rejection; ii) greater efficiency compared with techniques involving viral vectors or direct neuron transplantation; and iii) higher rates of neuron conversion and maturation compared to approaches that rely on injecting reprogramming growth factors [6].

Typically, fibroblasts exhibit a flat, spindle-shaped morphology [7], while neurons are highly polarized cells characterized by elongated processes (neurites), axons and dendrites. The elongation of fibroblasts during reprogramming reflects an early morphological transition associated with the loss of fibroblast identity and the acquisition of neuron-like features [2–8]. Although elongation alone is not sufficient to induce neuronal conversion, it often represents a preparatory step that sensitizes cells to transcription factors and small molecules driving full reprogramming. This structural transition involves extensive cytoskeletal and nuclear remodeling, which in turn modulates gene expression programs essential for establishing neuronal identity. In particular, the observed elongation is associated with actin cytoskeleton reorganization and activation of mechanosensitive signaling pathways known to regulate transcriptional activity [9].

Moreover, fibroblasts naturally express certain Transient Receptor Potential (TRP) channels, which are also widely found in neurons and play key roles in calcium homeostasis as well as mechanical and sensory transduction. This shared feature is particularly intriguing in the context of cellular reprogramming and offers a promising avenue for investigating sensory functions in induced neuronal systems [10–12].

Therefore, the development of faster, safer, and more efficient strategies to support neuronal reprogramming from fibroblasts is crucial for advancing novel approaches to study and treat neurological disorders [13–15].

In recent years, substrate topography at both micro- and nanoscale has emerged as a key biophysical cue capable of modulating cell morphology, including fibroblasts [16–18], and biomimetic hierarchical topographies have recently been shown to guide neuronal behavior, such as neurite outgrowth and alignment, using bioinspired anisotropic structures combined to conductive properties to promote directional growth and neural regeneration. [19–22]

In this context, exploiting the topographical cues of biomaterials to support fibroblast adhesion and proliferation, while promoting neuron-like morphological changes (e.g., projection elongation), may offer an effective tool for enhancing neuronal reprogramming outcomes [22,23].

Here, we investigated how fibroblasts morphological and structural responses to different biomaterial surfaces vary across species and age, two underexplored factors that may modulate cellular mechanosensitive through intrinsic differences in membrane composition, cytoskeletal organization, and mechanical properties. Our approach focused on guiding and controlling fibroblasts growth, adhesion and cytoskeletal organization by interfacing the cells with two different biomaterial substrates: silk fibroin (SF) and zinc aluminum hydrotalcite (ZnAl-HTlc) clays, both largely investigated for tissue-engineering. SF is particularly attractive due to its excellent biocompatibility, tunable mechanical properties and ability to form soft, nanostructured surfaces that mimic the elasticity of native ECM [24]. Previous studies have shown that SF hydrogels can integrate into brain tissue without inducing inflammation [22–26], while thin-film scaffolds based on methacrylate SF (FBMA) support neural cell survival and differentiation in models of neurodegeneration and brain injury [24]. Moreover, the influence of processing methods on the chemo-physical properties of SF film and their interaction with neural cells has been investigated, highlighting the potential use of SF interfaces in biocompatible electronic or photonic devices for advanced biomedical applications [26–30]. In contrast, HTlc clays provide a stiffer, more rigid substrate with well-defined nanoscale features and high mechanical resistance, ideal for probing fibroblast mechanosensitive. HTlc are biocompatible, do not trigger gliotic responses and have been shown to promote astrocyte differentiation via F-actin fiber alignment, positioning them as promising nanoscale interfaces for neural applications [31]. The topography and stiffness of SF and HTlc, both biocompatible, enable a comparative analysis of how fibroblasts perceive and respond to mechanical cues, crucial for designing substrates to support cell reprogramming and tissue regeneration.

As illustrated in Fig. 1, three types of fibroblast cultures were used in each experiment: rodent-derived fibroblasts (NIH-3 T3, hereafter referred to as MF) and primary human fibroblasts obtained from young (YHF) and elderly donors (EHF). The inclusion of aged human cells is particularly relevant, as fibroblasts retain age-associated epigenetic signatures, making them well suited for modeling late-onset neurodegenerative diseases such as Parkinson's and Alzheimer's [32]. To investigate the fibroblasts response to the SF and HTlc, we first assessed cell viability and cytoskeletal organization. We then performed a quantitative analysis of morphological changes across the three different groups, by measuring cell dry mass and projected area, and then evaluating the shape elongation in the three different group of fibroblasts. These parameters were extracted using label-free optical diffraction tomography (ODT) [33,34], an advanced imaging technique particularly well-suited for studying live-cell morphology in three dimensions (3D) [31,33–40]. ODT enables the non-invasive reconstruction of the refractive index (RI) distribution within biological samples, yielding high-resolution 3D images of cells without the need for labeling [36–38]. This technique offers precise quantification of cellular features such as volume, mass, and shape, revealing morphological changes associated with cell growth, mechanosensitive and early differentiation events, information that conventional 2D imaging techniques often miss [32,41–48].

In this study, we apply ODT technique to study the cell–material interface in a novel context, providing new data on how nanoscale surface features influence fibroblasts morphology. To our knowledge, this is the first detailed evaluation of fibroblasts morphological adaptation to biomaterial surfaces using ODT. Although this study does not directly address reprogramming, the parameters measured—cell mass and projected area, serve as key early, non-invasive indicators of cell state transitions, providing a foundation for future investigations into biomaterial-guided reprogramming.

2. Materials and methods

2.1. Fibroin substrate fabrication

Regenerated silk fibroin (SF) aqueous solutions were prepared from white cocoons of *Bombyx mori* silkworms (provided by CREA-API, Padua) following the protocol described in previous studies [49], with subsequent optimizations carried out at ISOF-CNR, Bologna. Briefly, the cocoons were degummed by autoclaving in water at 120 °C for 1 h. The resulting SF fibers were thoroughly rinsed with distilled water, dried, and then dissolved in a 9.3 M lithium bromide (LiBr) solution at 60 °C for 6 h. The obtained solution was dialyzed against distilled water for 48 h using cellulose acetate dialysis membranes (molecular weight cut-off: 12–14 kDa) and then centrifuged to remove any insoluble residues. The final regenerated SF solution, with a concentration of approximately 6 wt/vol%, was stored at 4 °C until use. For the preparation of silk fibroin (SF)-based films, 3 mL of a 5% aqueous fibroin solution were mixed with 20% glycerol (by weight relative to the protein). Glycerol was added to induce water insolubility of the protein, 70 μL of this mixture was subsequently deposited onto 19 mm diameter glass coverslips, to ensure reproducibility and uniform film thickness [49,50].

2.2. HTlc substrate fabrication

Colloidal aqueous dispersion of ZnAl-HTlc nanoparticles having the formula $[Zn_{0.72}Al_{0.28}(OH)_2]Br_{0.28}$ 0.69 H_2O were prepared by the

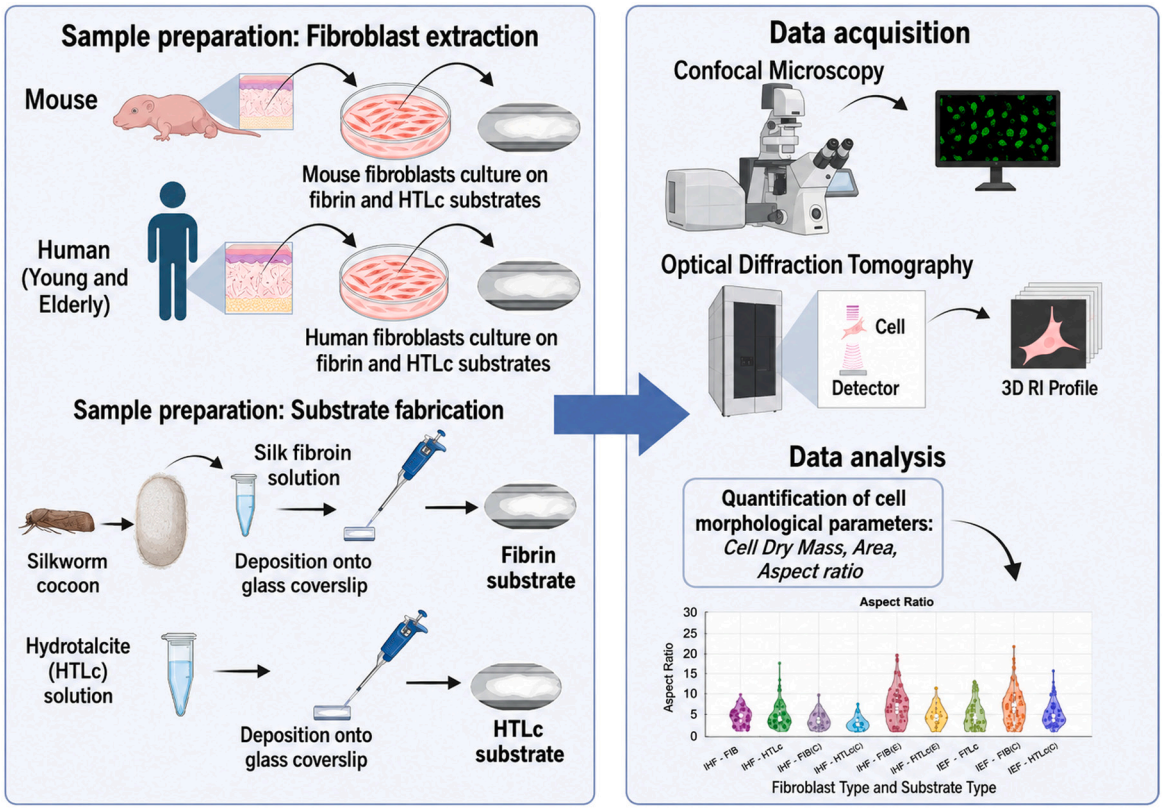

Fig. 1. Visual summary of the study.
Schematic overview of the study. Mouse and human (young and elderly) fibroblasts were extracted and cultured on fibroin, HTlc, and glass coverslip (used as control, CTRL). Fluorescent and confocal microscopy, ODT were performed to capture and quantify fibroblasts morphological parameters.

double-microemulsion technique as described [31], with a concentration of [1 mg/mL]. Then, HTlc films were prepared by drop casting the HTlc colloidal dispersion on 19 mm diameter glass coverslips and successively drying for 4 h in a sterile hood [31]. In this manuscript, the ZnAl-HTlc films will be referred to simply as HTlc.

2.3. Atomic Force Microscopy

The biomaterial surface was analyzed through Atomic Force Microscopy (AFM). Topographical images were acquired using an NT-MDT Solver scanning probe microscope operating in tapping mode, with samples maintained in air. Scans were performed at an oscillation amplitude of 50–60 nm, corresponding to 65% of the free amplitude at f_0. Image resolution was set to 512 × 512 pixels. The standard deviation of the average roughness was calculated from two independent 10 × 10 μm scans on three samples for each experimental condition.

2.4. Fibroblasts cell culture

The NIH-3 T3 cell line is one of the most widely used fibroblast cell models. In this study, it is referred to as mouse fibroblasts (MFs). Human dermal fibroblast (HDF) cultures, including both young and elderly human fibroblasts (YHFs and EHFs, respectively), were obtained at Bellaria Hospital (Bologna, Italy). Cells were derived from minimally invasive dermal skin biopsies of healthy donors provided by the University of Bologna, a procedure that resulted in only a small residual scar. They were subsequently transferred as small tissue fragments into 50 mL Falcon tubes and then placed in 36 mm Petri dishes containing 500 μL of medium. The tissue was then shredded into approximately 1 mm pieces using two scalpels and transferred to flasks together with the medium (DMEM - Dulbecco's Modified Eagle's Medium-, 10% FBS - fetal bovine serum, 1% penicillin-streptomycin, and 1% L-glutamine), ensuring complete coverage. The flasks were then placed into the incubator at 37 °C maintaining 95% humidified air and 5% CO2. Once fibroblasts had migrated out of the skin explants, the culture medium was replaced twice weekly to ensure an adequate supply of fresh nutrients. After approximately one month, primary human fibroblast cultures were established. When the cells reached ~90% confluence in the flask, they were passaged using 5 min trypsin-mediated detachment (Gibco-BRL), followed by 960 rpm for 5 min centrifugation and reseeding into new flasks. For experimental use, cells were plated onto the desired substrates upon reaching confluence in culture. Cekk concentration was determined using a Bürker chamber. The pellet obtained after centrifugation was resuspended in culture medium, and the required volume of cell suspension, corresponding to the target seeding density, was then plated onto the designated substrates. As a control, cells were seeded onto 15 mm glass coverslips.

2.5. Viability assay by fluorescein diacetate assay and Alamar Blue assay

The biocompatibility on CTRL, HTlc and SF films were analyzed by means of Fluorescein Diacetate assay (FDA), as described previously [31]. Cells were FDA-stained at room temperature (RT) for 5 min at 3 days in vitro (DIV). Fifteen different fields of about 0.6 × 0.6 mm were captured for each sample, using a Nikon ECLIPSE 80i microscope, equipped with appropriate fluorescence filters and a Nis-elements F300 CCD camera at lower and higher seeding density. Quantitative analysis was carried out by counting all the live (green) cells using Imagej software, discerning FDA-positive cells plated on CTRL, HTlc and SF substrates. Data is reported as mean ± SE of the N. of cells/area in histograms. Moreover, cell diameters were measured by using ImageJ software and data of cell diameters (μm) are reported as mean ± SE in histograms.

Cell viability was also quantitative evaluated using the Alamar Blue

assay (resazurin-based assay) and evaluated at two time points (6 and 10 DIV) the culture medium was replaced with fresh medium containing 10% (*v*/v) Alamar Blue reagent (Thermo Fisher Scientific, USA). Cells were incubated each time before the measurement for 4 h at 37 °C protected from light. The reduction of resazurin to the fluorescent resorufin product was quantified using a microplate reader (Varioskan, Thermo Fisher Scientific, USA) by measuring fluorescence (excitation 560 nm, emission 590 nm). All experiments were performed in at least three independent biological replicates, with each condition analyzed in technical triplicate.

2.6. Scanning electron microscopy

The morphology of the NHT-3 T3 cells and human fibroblasts was verified by a field emission scanning electron microscope (FESEM-ZEISS SIGMA 300) at an accelerating voltage of 5 kV. To observe the cells body, plated on the different substrates (CTRL, HTlc and SF), they were fixed with 2.5% glutaraldehyde at 4 °C, for 1 h. Each sample was then rinsed three times in PBS for 5 min before being stained 1 h in 1% Osmium Tetra-Oxide (OsO4) at RT; three further rinsing with distilled water were then performed. Then, the samples were sequentially dehydrated in 50%, 75%, 95%, and 99% ethanol. Dried specimens were coated with an evaporated gold (10 nm thickness) before analysis with the FESEM.

2.7. Structural cytoskeleton analysis by phalloidin staining confocal imaging and evaluation of TRPV1 expression

Cultured mouse and human fibroblasts plated on CTRL, HTlc and SF substrates were fixed in 4% paraformaldehyde (PFA), washed in (phosphate buffered saline) PBS, and permeabilized with 0.3% Triton X-100 in PBS. After blocking with 1% BSA in PBS, cells were incubated with Phalloidin-Rhodamine (Sigma-Aldrich, Milan, Italy) to label F-actin cytoskeleton filaments. Coverslips were mounted on slides, using a mounting medium (Thermofisher) and examined with a Nikon TE 2000 inverted confocal microscope equipped with 20× and 60× oil-objectives and 400 nm diode, 488 nm Ar^{+} and 543 nm He—Ne lasers as exciting sources. Fluorescent images of stained cells were also captured with Nikon Eclipse 80i fluorescent microscope and microscope Fluo-Spin up (Crisel Instruments) equipped with 20× and 40× objectives.

To evaluate the expression of TRPV1 for each sample, cells were washed twice with phosphate-buffered saline (PBS) and fixed with 4% paraformaldehyde for 15 min at room temperature (RT). After fixation, cells were permeabilized with 5% bovine serum albumin (BSA) in 0.1% Triton X-100 in PBS to prevent non-specific antibody binding. Cells were incubated overnight at 4 °C with a primary antibody against TRPV1 (Abcam), dilution (1:400) prepared in blocking solution. After three washes with PBS, samples were incubated with the appropriate fluorophore-conjugated secondary antibody (Cy3 anti-TRPV1) for 2 h. Nuclei were counterstained with mounting solution containing DAPI (1 μg/mL). Samples were examined by fluorescence microscope. Images were acquired under identical exposure and acquisition settings for all experimental groups. For the analysis and evaluation of results, at least 10 randomly selected fields per sample were imaged.

2.8. Optical diffraction tomography (ODT) and sample preparation

MF, YHF, and EHF cells seeded on CTRL, HTlc, and SF films were fixed with 4% PFA, washed with PBS, and imaged using both 3D refractive index (RI) tomography and 2D maximum intensity projection (MIP) after acquisition with both HT-2 (Schaefer SEE srl, Italy; Tomocube, Republic of Korea) and the HT-X1 system (JHU, Tomocube, Republic of Korea) after 5 DIV from the plating. Image acquisition techniques were developed to accurately delineate cells boundaries and to capture fine processes of cells body. Data were visualized using Maximum Intensity Projection (MIP) images that displays 3D data in 2D, showing only the brightest, highest-density structures from a series of volumetric images by projecting the maximum intensity value along each ray into a single 2D image.

These systems are comprised of i) a motorized stage, a 60×, 1.2 NA water-immersion objective, a 532 nm laser, and a dynamic micro mirror device, that measures the 3D refractive indexes ii) a 40×, 0.95 NA air objective and a 450 nm LED light source.

2.9. Morphological analysis of ODT images

Segmentation of individual fibroblasts was performed manually on 2D MIP images using ImageJ. Following segmentation, approximately 40 fibroblasts were obtained per sample type. These 2D segmented masks were then applied to the corresponding 3D RI tomogram stacks to reconstruct single-cell 3D RI tomograms, isolating one cell per field of view [43,44,49–51]. In contrast, the original 3D RI tomograms typically contained multiple cells.

Quantitative analyses were performed on single-cell 3D RI tomograms using MATLAB. Cell area was calculated by counting the number of non-zero pixels within the segmentation masks. Cell dry mass was determined by applying refractive index thresholds and computing the surface integral of the optical path difference, using the specific refractive index increment [44]. The aspect ratio was obtained by fitting an ellipse to each cell and calculating the ratio between the major and minor axes.

2.10. Solutions and chemicals

All salts and chemicals employed for the investigations were of the highest purity grade (Sigma Aldrich). For viability FDA experiments and ODT Imaging, the standard bath saline was (mM): 140 NaCl, 4 KCl, 2 MgCl2, 2 CaCl2, 10 Hepes, 5 glucose, pH 7.4 with NaOH and osmolarity adjusted to 315 mOsm with mannitol.

2.11. Statistical analysis

Statistical Analysis is reported as the mean average ± standard error (S.E.). Each experiment was performed, at least in triplicate three times, on different batches of cells, plated on both CTRL and HTlc and SF substrates. The analyses and statistics were performed with Origin Micro Cal Ver 6.0. Data were compared by one-way ANOVA with Bonferroni post-test or student's t-test. * $p < 0.05$, ** $p < 0.01$, *** $p < 0.001$ independent t-test.

3. Results and discussion

We explored the potential of biomaterials substrates to promote the development of neuron-like morphological features from fibroblasts of different species and age groups. The effects of organic (SF) and inorganic (HTlc) biomaterials on cell viability, adhesion, and morphological differentiation were evaluated.

3.1. SF and HTlc substrates fabrication and characterization

Fig. 2 shows, respectively, the two tested biomaterials: SF (Fig. 2A) film and HTLc (Fig. 2B) film deposited on 1) glass coverslips by drop-casting solutions containing proteins derived from *silk Bombyx mori* [52] and 2) colloidal aqueous dispersion of ZnAl-HTlc nanoparticles [31]. The films are both optically transparent, a fundamental prerequisite for ODT measurements. Atomic force microscope (AFM) images (right panels of Fig. 2A and B) highlight a pronounced morphological contrast between the two coatings: SF exhibits a smooth surface (RMS roughness ≈ 5 nm), while HTlc is considerably rougher (RMS roughness ≈ 125 nm). This nearly two-orders-of-magnitude difference in roughness, together with the intrinsically different mechanical nature of the two materials, provides a robust platform to compare two markedly

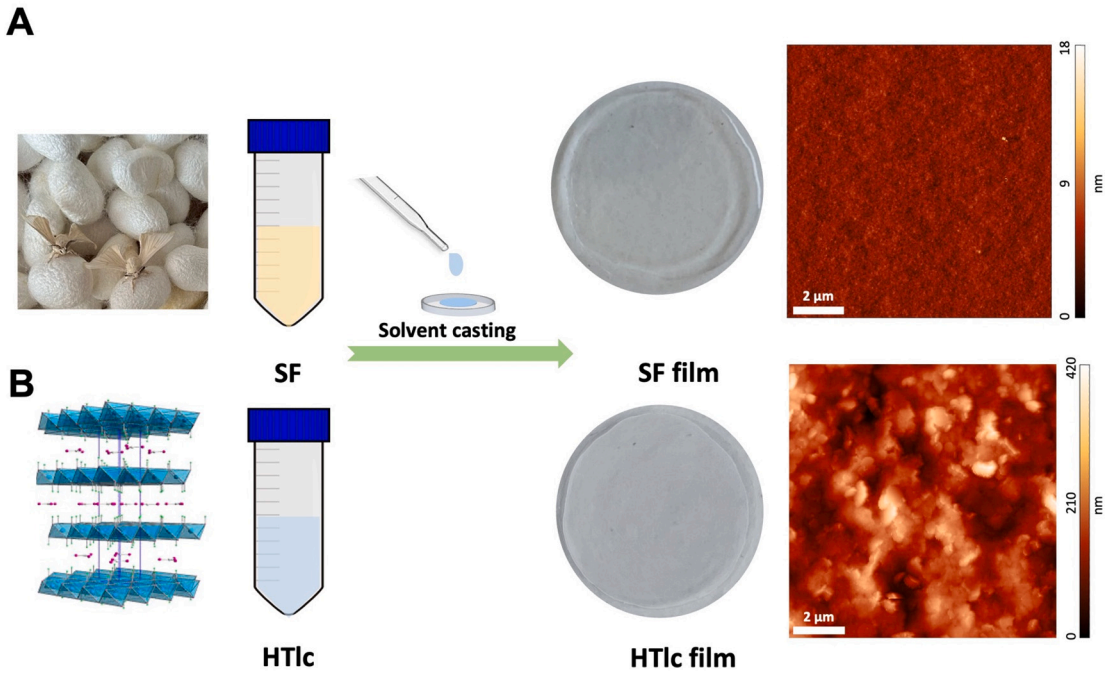

Fig. 2. Structure and AFM substrates.
Schematic representation of the SF and HTLc film synthesis and surface characterization. **A)** *Silk Bombyx mori* (left panel), a photograph of the free-standing SF film, and the corresponding AFM image of its surface (right panel). **B)** ZnAl-HTlc structure (left panel), the drop-cast ZnAl-HTlc film and the related AFM image of its surface (right panel). The SF film exhibits a smooth and homogeneous surface with low roughness, whereas the HTlc film shows markedly higher surface roughness with aggregated nanostructures.

different classes of biomaterials and to evaluate how interfacial physical cues, topography and mechanics, guide fibroblast adhesion, growth, proliferation and morphology.

3.2. Cell biocompatibility, growth and proliferation on SF and HTlc substrates

Building on previous studies demonstrating that SF and HTlc promote cell growth and network dynamics [31,52], we evaluated their biocompatibility and capacity to support fibroblast adhesion, growth, and proliferation. Experiments were conducted using both mouse and human fibroblasts, including cells derived from healthy young and elderly donors. Results were systematically compared with those obtained on standard glass coverslip substrates, used as the control condition (CTRL).

Cell viability was assessed after 3 DIV using the fluorescein diacetate (FDA) assay. Live cells were visualized by fluorescence and confocal microscopy (Nikon Eclipse 80i, 20 × −50× objectives), allowing both viability evaluation and morphological analysis (Fig. 3L–T and Fig. S1).

Scanning electron microscopy (SEM; Fig. 3A–I and Fig. S2) further complemented the imaging analyses, providing high-resolution insights into cell–substrate interactions. As shown in Fig. 3, all fibroblast types exhibited effective adhesion and proliferation on both SF and HTlc substrates, comparable to the control condition (CTRL). Notably, mouse fibroblasts (MFs), despite displaying a smaller and more rounded morphology, showed robust viability, proliferation, and spreading on both substrates. These observations were further supported by low-density imaging (Fig. S1A, D, G), which highlighted enhanced cell adhesion on SF and HTlc compared with the CTRL. YHFs also adhered and proliferated efficiently on both substrates; however, they exhibited a distinct morphological response. In particular, YHFs displayed a significantly increased elongation on SF and HTlc relative to the CTRL (Fig. 3 P, S). This effect was particularly evident in lower-magnification images (Fig. S2 E, H), suggesting that substrate properties modulate cellular elongation in YHF. SEM imaging (Fig. 3A-I) provides detailed visualization of cytoplasmic extensions and spatial organization of the cells on biomaterial surface. These findings align with ongoing research into the development of fibroin-based materials, including peptide-functionalized SF hydrogels, aimed at promoting tissue regeneration, such as the possible applications in brain repair [53,54].

In contrast, EHFs showed limited elongation of cell body on the SF surface, compare to YHFs (Fig. 3 T and Fig. S1I), with only a modest increase in adhesion on HTlc surface compared to CTRL (Fig. 3 Q and Fig. S1C, F) and a notable elongation, indicating that HTlc may enhance cellular responsiveness even in aged cells, despite their reduced proliferative capacity.

Numerical analysis was performed and reported as histograms in Fig. 3U-Y. Fig. 3U, V show the number of cells per area, while Fig. 3X, Y show the measurements of cell diameters. Both density and average diameter revealed differences in cell behavior depending on substrate chemistry and surface topography. Fibroblasts from both mouse and human cultured on HTlc showed similar spreading, with the effect being more pronounced in both YHFs and EHFs (dark gray and light gray bars, Fig. 3U, V). Conversely, the number of MFs adhering to SF was comparable to CTRL (Fig. 3U), whereas EHFs showed a significant lower density compared to both CTRL and HTlc (dark gray and light gray bars, Fig. 3U, V). These findings indicate that HTlc robustly supports fibroblast adhesion and proliferation. In contrast, while SF remains biocompatible, it elicits a more variable cellular response, particularly in aging cells, likely due to differences in interfacial cues arising from its free-standing film preparation. As demonstrated by AFM in Fig. 2, HTlc show a surface with high roughness with the presence of larger features, peaks and depressions that create a complex surface that can significantly enhance biological adhesion, by providing more physical anchoring sites and expanding the effective surface area, available for biomolecular attachment. This type of topography can facilitate the formation of focal adhesion points for cells or improve protein adsorption through enhanced mechanical interlocking and local energy minimum. In contrast, SF surface is characterized by a lower roughness and highly uniform topography that may reduce the ability of biomolecules

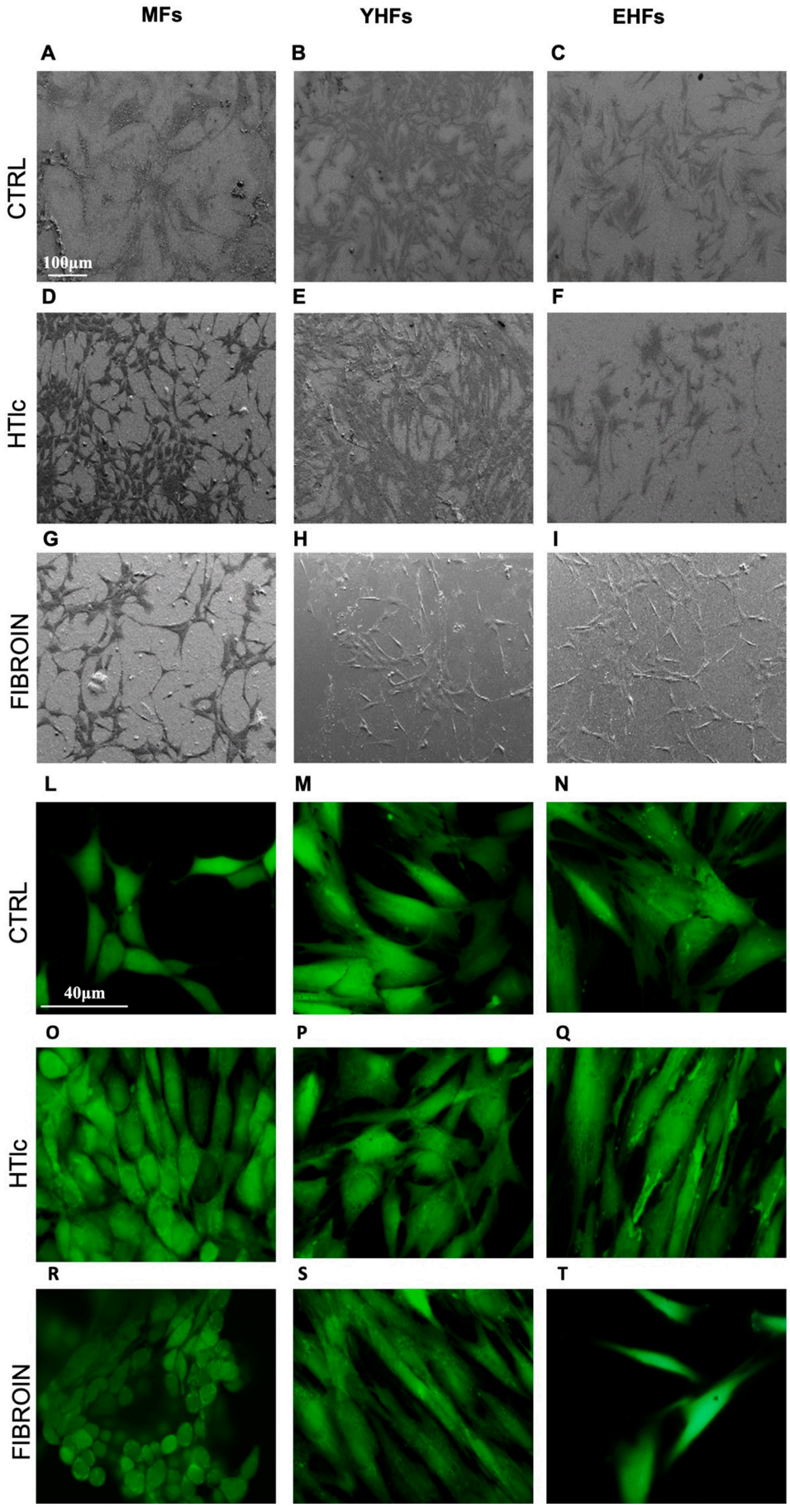
MFs
YHFs
EHFs
A
B
C
CTRL
100µm
D
E
F
HTIc
G
H
I
FIBROIN
L
M
N
CTRL
40µm
O
P
Q
HTIc
R
S
T
FIBROIN

Fig. 3. SEM on the substrates.
SEM images of MF (A, D, G), YHF (B, E, H) and EHF (C, F, I) cultured on CTRL (A-C), HTlc (D-F) and SF (G-I) substrates. Scale bars, 100 μm. Note the presence of elongated morphology of human fibroblasts compared to the flatter and small structure of mouse cell bodies. Moreover, YHFs and EHFs show elongated branches on HTlc (E, F) that follow the rod like structure of the substrate itself. Impressive is the higher cell number of YHFs on HTlc (E) compared to CTRL (B) and SF (H). Fluorescent green images on the right panel of low density seeding of MF (L, O, R), YHF (M, P, S) and EHF (N, Q, T) stained with FDA for glass CTRL (L-N), HTlc (O-Q) and SF (R-T). Scale bars, 40 μm. Histograms (U, X) reporting the analysis of the number of cells/area and cell diameter measurements on MFs (X) and both YHFs and EHFs (V, Y). Data are presented as mean ± SE. Statistical significance was calculated via one-way analysis of variance (ANOVA) with Bonferroni post-test. *P* values are reported in the graph when $P \leq 0.05$.

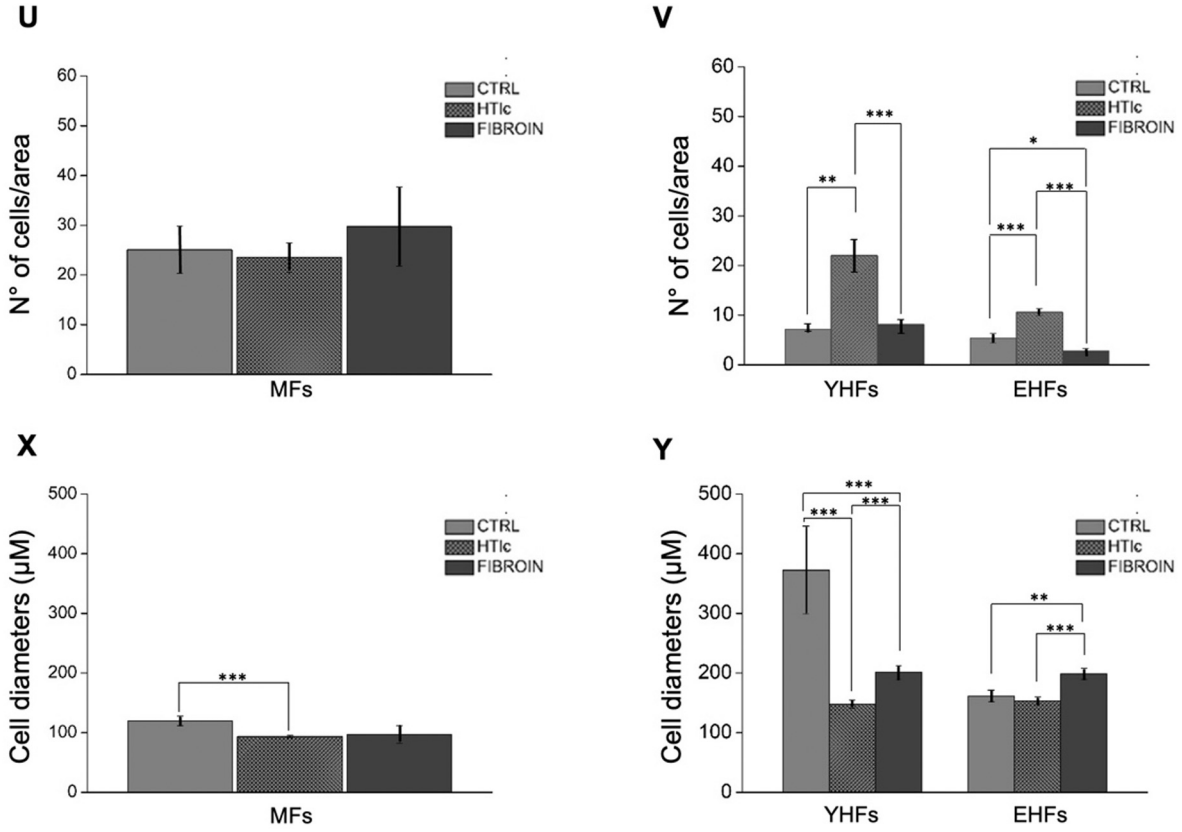

Fig. 3. (*continued*).

to mechanically interact and promote cells adhesion.

In addition, cell body diameters were measured to evaluate morphological adaptation and differentiation, particularly cell elongation in response to different substrate chemistry and topography (Fig. 3X, Y). In MFs, the average cell diameter significantly decreased on HTlc compared to CTRL, while no significant change was observed on SF (Fig. 3X). On the other hand, YHFs exhibited a significant reduction in cell diameter on both HTlc and SF, indicating enhanced morphological plasticity on these substrates. This reduction in diameter aligns with the increased cell body elongation, driven by the substrate properties of HTlc and SF compared to CTRL (Fig. 3Y). Conversely, EHFs showed little change in diameter on HTlc compared to CTRL, whereas a significant increase on SF compared to both HTlc and CTRL, suggesting a distinct response of aging cells to SF surfaces. Data were analyzed using one-way ANOVA with Bonferroni's test. A significance threshold of $p < 0.05$ was applied, and all results are reported as mean ± standard error of the mean (SEM).

To evaluate the ability of the different substrates to support cell survival over longer time, cell metabolic activity was assessed by Alamar Blue assay (Fig. S3) at 6 and 10 DIV in MFs, YHFs and EHFs cultured on CTRL, HTlc, and fibroin substrates. All substrates are alive and proliferate, confirming the substrates overall cytocompatibility at longer time. As expected, MFs displayed a markedly higher proliferative capacity than both human fibroblast populations, with a substantial increase in metabolic activity between 6 and 10 DIV, particularly on CTRL and HTlc substrates. YHFs showed a moderate increase in proliferation over time, whereas EHFs exhibited the lowest metabolic activity, consistent with their reduced proliferative potential associated with donor age. Notably, cells cultured on Fibroin, generally exhibited lower proliferation rates compared with Control and HTlc conditions, suggesting that this substrate may limit fibroblast expansion while still maintaining cell viability. However, especially at 10 DIV EHFs maintain a modest viability on fibroin compare to HTlc, confirming what SEM and fluorescent microcopy revealed already a 3 DIV.

3.3. Morphological characterization using phalloidin staining

Actin filaments are central to a range of cellular processes, including migration, adhesion and mechanotransduction and their architecture reflects the cell ability to sense and adapt to substrate cues. To investigate cytoskeletal organization in response to substrate topography, fibroblasts cultured on CTRL, HTlc and SF substrates were stained using rhodamine phalloidin (Fig. 4), which specifically binds filamentous actin (F-actin, red). Hoechst (blue) was used to label cell nuclei, (Fig. 4A-F). We note that the identification of nuclei for the cells cultured on SF was occasionally hindered due to substrate autofluorescence (Fig. 4G-I). This dual staining approach therefore enabled the visualization of actin cytoskeleton remodeling and associated morphological rearrangements under the different culture conditions.

Confocal images in Fig. 4, showing the phalloidin staining at 4 DIV,

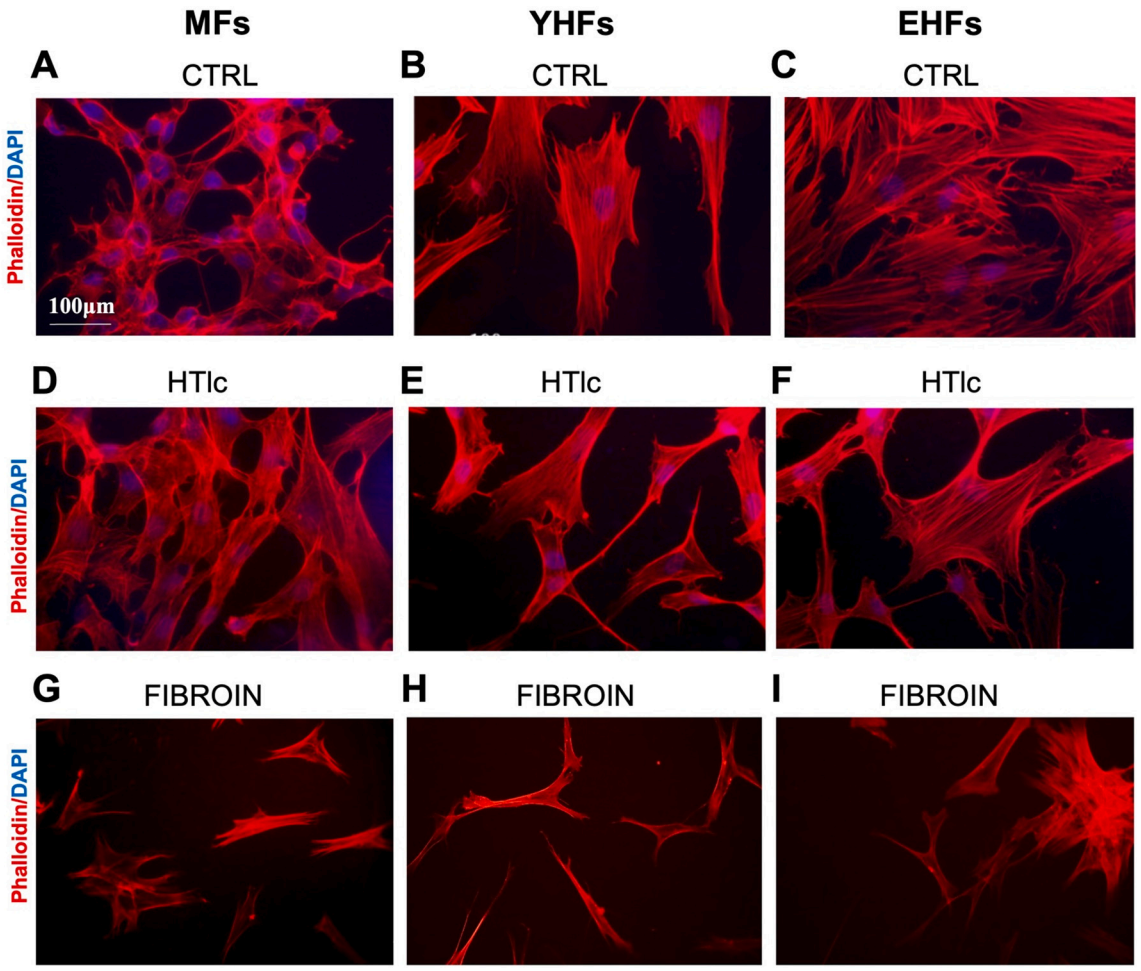

Fig. 4. Confocal microscopy.
Confocal micrographs (A-I) representing different MF (A, D, G), YHF (B, E, H), and EHF (C, F, I) stained for actin (red) and DAPI (blue) grown on CTRL (A-C), HTlc (D-F) and SF (G-I) substrates. Scale bars, 100 µm.

revealed striking differences among substrates. Both mouse and human fibroblasts displayed sparse distribution, typical of fibroblasts in vitro on CTRL (Fig. 4A–C). Consistent with the FDA assay data (Fig. 3), mouse fibroblasts (Fig. 4A) exhibited smaller cell bodies compared with the flatter, spindle- or star-shaped morphology observed in human cells (Fig. 4B, C). This finding is consistent with well-known intra-species differences in cytoskeletal and spreading organization.

On HTlc substrates (Fig. 4D–F), both murine and human fibroblasts formed dense cellular clusters characterized by pronounced elongations and numerous protrusive structures, indicative of active cytoskeletal remodeling and potential intercellular networking. These protrusions likely reflect enhanced cell–cell interactions promoted by the increased surface roughness of HTlc, which may foster cell network dynamics. Such behavior is commonly associated with strengthened cell adhesion and mechanotransduction processes [55].

Age-related alterations in cytoskeletal architecture were also evident. Fibroblasts from EHFs (Fig. 4C, F, I) displayed less pronounced actin filament organization and reduced elongation, relative to those from younger donors (Fig. 4B, E, H), when cultured on biomaterial substrates. These differences may reflect age-associated changes in cellular stiffness or reduced mechanosensitive. Indeed, aging has been linked to the accumulation of stress fibers, impaired actin turnover, and decreased responsiveness to topographical cues, all of which can affect cell morphology and function [3,4,7].

Interestingly, cells cultured on SF exhibited substrate-specific actin architectures distinct from both CTRL and HTlc. Across all fibroblast types, actin filaments on SF appeared less organized into stress fibers and more diffusely distributed (Fig. 4G–I). This suggests a more moderate spreading behavior and potentially a distinct mode of cytoskeletal engagement with the substrate. Unlike the prominent, directionally aligned stress fibers observed on HTlc, actin structures on SF were more concentrated in specific areas, aligned in unidirectional bundles [56].

Taken together, these findings demonstrate that HTlc elicited the strongest cytoskeletal remodeling and network formation.

To further explore whether the substrate-dependent changes in cytoskeletal organization were associated with the modulation of mechanosensitive pathways, TRPV1 expression was evaluated by immunofluorescence in MFs, YHFs and EHFs cultured on CTRL, HTlc, and SF substrates (Fig. 5). TRPV1 is a non-selective cation channel traditionally associated with sensory neurons and nociceptive signaling, but accumulating evidence indicates that it is also expressed in fibroblasts, where it participates in calcium homeostasis, mechanotransduction, inflammatory responses, and extracellular matrix remodeling [10–12]. Data show fibroblasts cultured on HTlc (Fig. 5 D-F) and, more prominently, on SF substrates exhibited a more elongated and polarized morphology, characterized by thin cellular extensions and spindle-like profiles, mirroring the cytoskeletal rearrangements observed by phalloidin staining (Fig. 5 G-I). Under these conditions, TRPV1 labeling appeared to be increased relative to CTRL cultures, particularly in MF (Fig. 5A) and YHFs (Fig. 5B), whereas EHFs (Fig. 5C) displayed a more heterogeneous staining pattern with less evident enhancement.

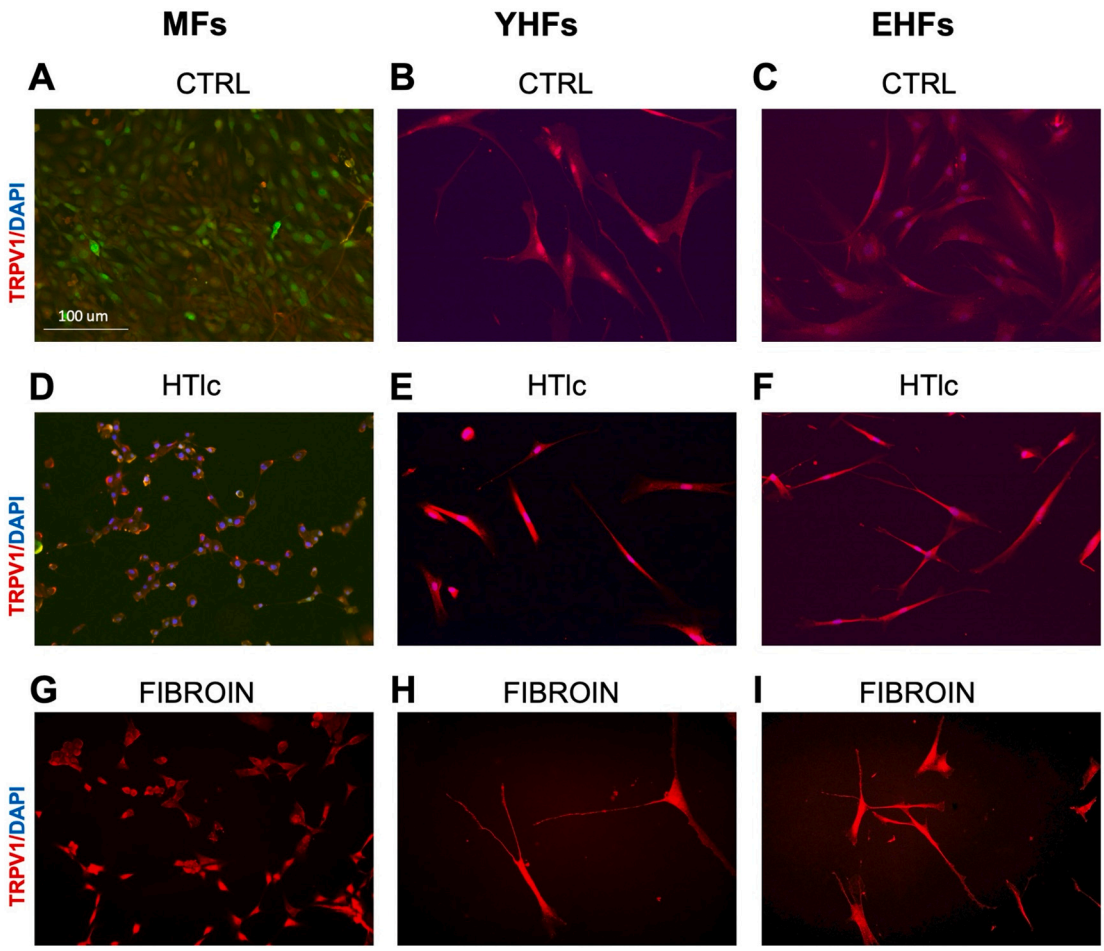

Fig. 5. TRPV1 immunofluorescence.
TRPV1 immunofluorescence in MF and HF cultured on different substrates. Representative immunofluorescence images of TRPV1 expression in mouse fibroblasts (MFs; A, D, G, green +GFAP)), young human fibroblasts (YHFs; B, E, H), and elderly human fibroblasts (EHFs; C, F, I) cultured under control conditions (CTRL; A–C) or on HTlc (D–F) and fibroin (G–I) substrates. Scale bars: 100 μm.

In conclusion, the apparent association between substrate-induced morphological adaptation and increased TRPV1 expression suggests that this channel may contribute to fibroblast sensing of extracellular physical cues in a species- and age-dependent manner and support the emerging concept that fibroblasts share with sensory neurons conserved molecular mechanisms of environmental sensing.

3.4. Optical Diffraction Tomography (ODT) to reveal differentiated cells properties

To quantify the morphological changes induced by the different substrates across various fibroblast types, we performed ODT observations of MFs, YHFs and EHFs cultured on CTRL, HTlc and SF substrates. ODT provided high-resolution, label-free 3D RI maps of individual cells; representative maximum intensity projection (MIP) images are shown in Fig. 6. On all substrates, cells exhibited visible differences in shape and RI distribution, in agreement with those qualitatively observed in the SEM, FDA and phalloidin analyses describes in previous sections. On CTRL substrate (Fig. 6A–C), fibroblasts are more spread, while on HTlc (Fig. 6D–F) and SF (Fig. 6G–I) substrates cells are more elongated or anisotropic.

These visual trends were most evident in the YHFs, though variability was observed across all cell types and substrates. The RI mapping highlighted potential differences in cellular organization, which were further examined through quantitative analysis in Fig. 7. Fig. 7A–C shows ODT-based quantification of fibroblast dry mass, cell area, and aspect ratio across the different cell types and substrates. Fig. 7A shows that cell dry mass was comparable for YHFs and EHFs across all substrates, ranging between approximately 200 and 400 pg. In contrast, MFs exhibited a mean dry mass of ~200 pg when cultured on CTRL and SF substrates, with a modest increase to ~300 pg when cultured on HTlc. Since substrate stiffness is known to influence cell behaviors like migration, adhesion, and proliferation, these effects may indirectly affect cell dry mass [57–59]. Changes in cell dry mass can also reflect alterations in cell metabolism and viability [60].

Fig. 7B quantifies cell area. Both YHFs and EHFs exhibited the largest area when cultured on CTRL compared to HTlc and SF substrates, and relative to MFs. Notably, YHFs on CTRL displayed the largest cell area, significantly surpassing all other conditions. Cell area decreased on HTlc and was smallest on SF, regardless of fibroblast type. These data indicate increased cell body elongation, consistent with fluorescent microscopy observation (Fig. 6). This trend was observed across MFs, YHFs and EHFs, although EHFs generally showed smaller cell areas compared to YHFs.

Fig. 7C measures the aspect ratio, reflecting cell elongation. YHFs and EHFs cultured on HTlc demonstrate the highest aspect ratio, indicating the most pronounced elongation, followed by SF and glass. MFs exhibit the lowest aspect ratio on all substrates compared to YHFs and EHFs. These results highlight the role of substrate properties in dictating cell shape, with glass (CTRL) favoring spread out morphologies, while SF inducing more compact, rounded shapes, and HTlc promoting elongated morphology. Noteworthy, the dry mass of all cells is comparable

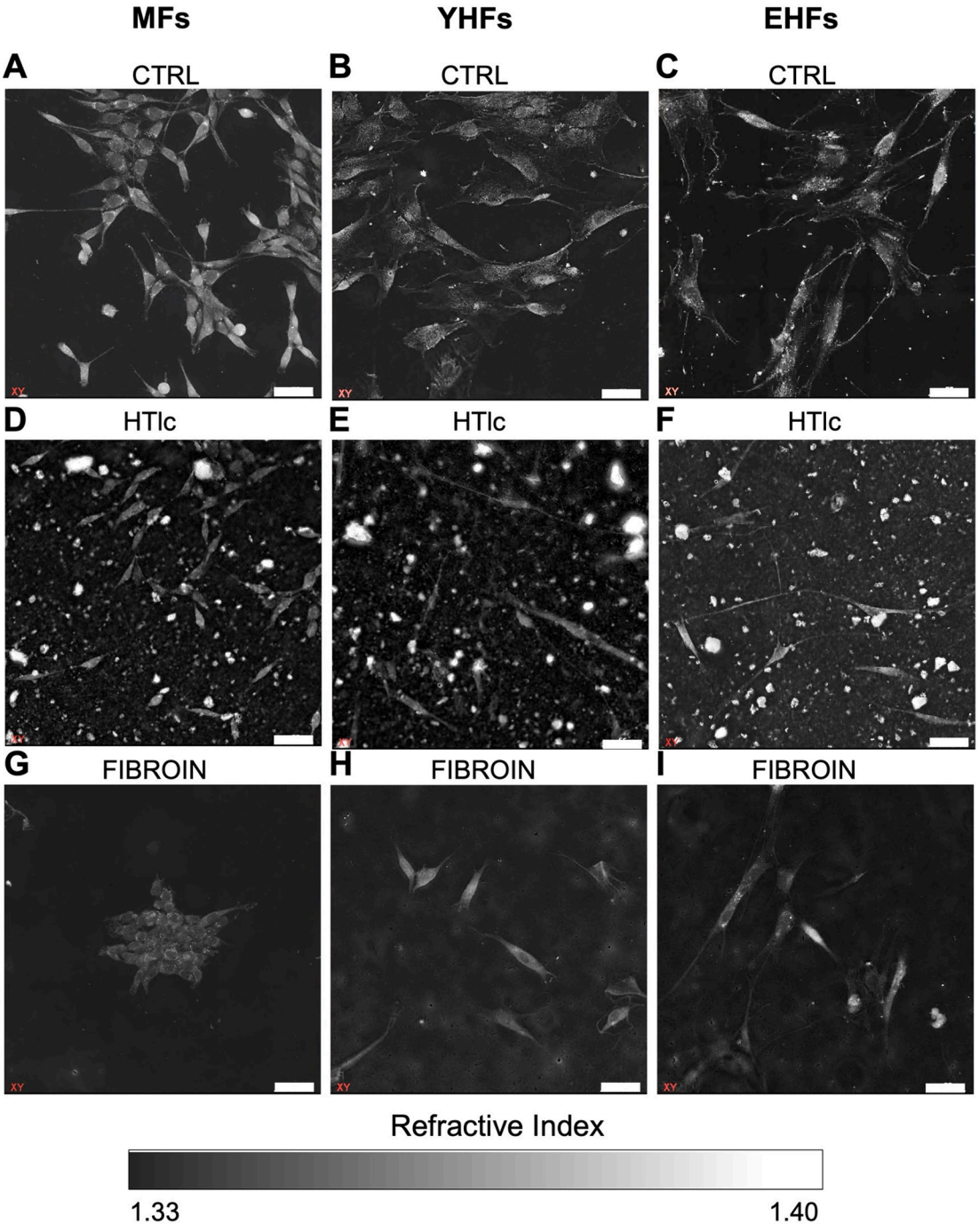

Fig. 6. ODT.
ODT images of MF (A, D, and G), YHF (B, E, and H) and EHF (C, F, and I) cultured on CTRL (A-C), HTlc (D-F), and SF (G-I). Scale bar: 50 μm. Legend indicates RI value range. CTRL (A-C) promoted maximal adhesion, spreading, and cytoskeletal organization, as shown by the uniform RI distribution. Fibroblasts cultured on HTlc (D-F) and SF (G-I) appeared to have an elongated morphology, with more emphasis on the latter. The RI mapping provides critical insights into how substrate properties influence cellular morphology and can be used to quantify those morphological parameters.

throughout the groups, but the cell area differs significantly, indicating that the fibroblasts on HTlc and SF are denser than the ones on glass.

Overall, our results indicate that human fibroblasts, both YHFs and EHFs, exhibit a more pronounced responsiveness to surface cues compared to MFs, which showed limited qualitative and quantitative changes. Among the biomaterials analyzed, HTLc substrates were the most effective in promoting fibroblast elongation, a morphological feature commonly associated with neuron-like cellular architecture. As expected, EHFs displayed reduced proliferative capacity and lower plasticity compared to YHFs; nevertheless, our findings demonstrate that fibroblasts derived from elderly donors can still be guided toward neuron-like morphological features through appropriate substrate design. This observation is particularly relevant for disease modeling approaches targeting late-onset neurodegenerative conditions, where patient-derived cells from aged individuals represent a critical and clinically meaningful resource. In this context, the quantitative assessment enabled by ODT allowed these substrate- and age-dependent morphological differences to be objectively evaluated through parameters such as cell dry mass, area, and aspect ratio, providing a robust and unbiased framework to evaluate fibroblasts remodeling.

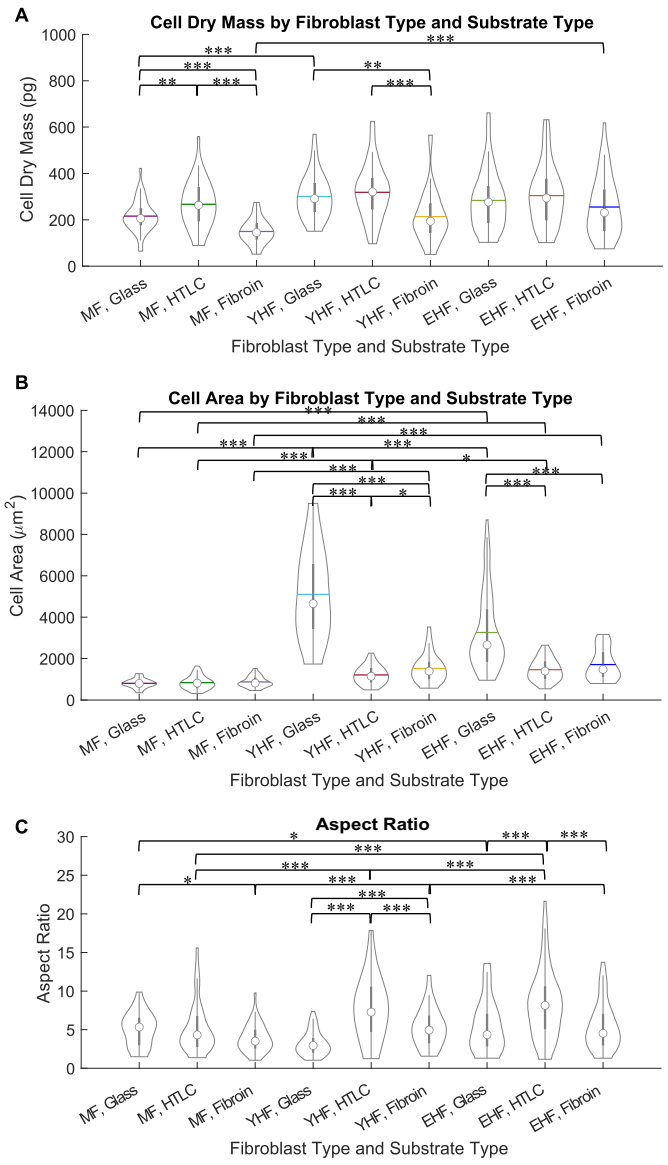

Fig. 7. Quantification of ODT data.
Quantification of morphological parameters (A) Cell dry mass, (B) Cell area, and (C) aspect ratio, for mouse (MF), young human fibroblasts (YHF), and elderly human fibroblasts (EHF), cultured on different substrates (CTRL, HTlc, and SF). (*$p \leq 0.01$, **$p \leq 0.001$, ***$p \leq 0.0001$).

4. Summary and perspectives

Here, we investigated whether the behavior and morphological remodeling of three different types of fibroblasts could be modulated using two distinct interfaces: SF, an organic, soft and relatively smooth substrate that partially mimics the elasticity of native ECM; HTlc, an inorganic, stiffer and rougher substrate that provides stronger topographical and mechanical cues. Our results show that these substrates significantly affect fibroblast adhesion, proliferation, shape and cytoskeletal organization. HTlc promoted good adhesion and proliferation, while fostering marked cell elongation extensive protrusions and F-actin fiber alignment, suggesting enhanced cell–substrate and cell–cell interactions driven by its rough surface. This mechanosensitive response was age-dependent, being more evident in young rather than elderly human fibroblasts. SF also supported fibroblast shape remodeling, promoting elongation and cytoskeletal reorganization, although its effects were generally less pronounced than those observed on HTlc.

Table 1 provides an overview of the results obtained across all substrates, as described in detail in the previous section.

In this context, our study represents an important step toward translational application of cell conversion strategies by combining biomaterials commonly used for tissue repair and regeneration with label-free 3D optical imaging to investigate fibroblast morphological remodeling. To our knowledge, this is the first study to quantitatively assess species- and age-dependent fibroblast morphology on biomaterials using ODT through parameters such as cell dry mass, projected area and aspect ratio. These descriptors provide non-invasive indicators of cellular organization and may help identify early morphological signatures associated with cell-state transitions.

Future developments should aim to integrate biomaterial-derived mechanical cues, with biochemical reprogramming strategies including transcription factors, small molecules or growth-factor-based protocols, to determine whether substrate-induced morphological remodeling can enhance conversion efficiency and neuronal maturation. Furthermore, the development 3D biomaterial scaffolds with controlled stiffness and nanoscale topography will be crucial to better mimic the evolving mechanical environment of the nervous system and to optimize reprogramming efficiency by recapitulating the complexity of the in vivo microenvironment.

A key challenge will be to establish a direct link between early morphological changes, such as elongation, cytoskeletal alignment and dry-mass redistribution, and the functional acquisition of neuronal or glial phenotypes. Addressing this limitation will require combining ODT-based morphological analysis with molecular markers of neuronal identity, transcriptomic profiling, and electrophysiological measurements to validate functional maturation.

Moreover, the integration of label-free techniques such as ODT with machine-learning approaches could further enable the identification of predictive morphological signatures, allowing early selection of responsive cells. In a translational perspective, these strategies may be particularly relevant for patient-derived fibroblasts from aged donors, which are essential for modeling late-onset neurological disorders. Overall, combining engineered biomaterials, quantitative label-free imaging and reprogramming protocols may provide a powerful framework for advancing personalized regenerative medicine and disease modeling in the nervous system.

5. Conclusion

In conclusion, this study demonstrates that biomaterial interfaces with finely tuned mechanical and topographical properties can

Table 1
Comparison of the effect of the different substrates on different properties of fibroblast cells.

Murine fibroblast (MFs)	Glass CTRL	Silk Fibroin SF	Hydrotalcite HTlc
Cells/area	+	+	+
Diameter	+++	-	-
Elongation	-	+	+
Cytoskeleton reorganization	-	+	++
Human fibroblast (YHFs)	**Glass CTRL**	**Silk Fibroin SF**	**Hydrotalcite HTlc**
Cells/area	+	+	+++
Diameter	+++	+	-
Elongation	+	++	+++
Cytoskeleton reorganization	-	+	++
Human fibroblast (EHFs)	**Glass CTRL**	**Silk Fibroin SF**	**Hydrotalcite HTlc**
Cells/area	+	+	+++
Diameter	+	+	+++
Elongation	+	+	++
Cytoskeleton reorganization	-	+	+

modulate fibroblast morphology and cytoskeletal organization in a species- and age-dependent manner. By integrating well defined organic and inorganic substrates with quantitative, label-free ODT, we establish a powerful platform to capture early, mechanosensitive morphological signatures that precede functional cell-state transitions. Importantly, our results highlight surface roughness and stiffness as critical design parameters capable of directing cell elongation, protrusive activity, and cytoskeletal alignment, features to identify cellular plasticity. These findings provide a rational basis for the design of advanced biomaterial systems aimed at enhancing cell reprogramming and promising framework for advancing personalized regenerative medicine and biomaterial-based disease models.

CRediT authorship contribution statement

Francesco Formaggio: Writing – review & editing, Formal analysis. **Pooja Anantha:** Writing – review & editing, Methodology. **Federica Trebbi:** Methodology, Investigation, Formal analysis. **Vincenzo Palermo:** Writing – review & editing, Writing – original draft, Methodology, Conceptualization. **Tamara Posati:** Writing – review & editing, Methodology. **Marianna Barbalinardo:** Methodology. **Gioacchino Calandra Sebastianella:** Writing – review & editing, Supervision, Formal analysis, Data curation. **Simone Bonetti:** Methodology. **Marco Caprini:** Writing – review & editing. **Jessica Chen:** Data curation. **Giovanna Sotgiu:** Methodology. **Maira Bacchiega:** Methodology. **Roberto Zamboni:** Methodology. **Annalisa Convertino:** Writing – original draft, Supervision, Funding acquisition, Data curation. **Ishan Barman:** Writing – review & editing, Supervision, Methodology, Data curation. **Emanuela Saracino:** Writing – review & editing, Writing – original draft, Visualization, Validation, Supervision, Software, Resources, Project administration, Methodology, Investigation, Funding acquisition, Formal analysis, Data curation, Conceptualization.

Uncited references

[18a,18b,18c]

Declaration of competing interest

The authors declare that they have no competing financial interests or personal relationships that could have influenced the work reported in this study.

Acknowledgments

E.S. acknowledge the financial support from PNRR MUR project ECS_00000033_ECOSISTER and CNR Grant Short Term Mobility for DSCTM (STM 2023) and MUR FISA-2023-00346. E.S., V.P. thanks Schaefer Italy (https://www.schaefer-tec.it/it) to support the work with the HT-2 QPI Tomocube Instrument. E.S., A.C and I.B. thank the Italian National Council Research–Johns Hopkins University Joint Laboratory "Integrating Transparent Nanowires in Optical Diffraction Tomography to Investigate Collective Cell Behaviour".

Appendix A. Supplementary data

Supplementary data to this article can be found online at https://doi.org/10.1016/j.bioadv.2026.215063.

Data availability

Data will be made available on request.

References

[1] J.H. Wang, G. Yang, Z. Li, W. Shen, Fibroblast responses to cyclic mechanical stretching depend on cell orientation to the stretching direction, J. Biomech. 37 (4) (2004 Apr) 573–576, https://doi.org/10.1016/j.jbiomech.2003.09.011 (PMID: 14996570).
[2] T. Vierbuchen, A. Ostermeier, Z.P. Pang, Y. Kokubu, T.C. Südhof, M. Wernig, Direct conversion of fibroblasts to functional neurons by defined factors, Nature 463 (7284) (2010 Feb 25) 1035–1041, https://doi.org/10.1038/nature08797 (Epub 2010 Jan 27. PMID: 20107439; PMCID: PMC2829121).
[3] M.V. Plikus, X. Wang, S. Sinha, E. Forte, S.M. Thompson, E.L. Herzog, R.R. Driskell, N. Rosenthal, J. Biernaskie, V. Horsley, Fibroblasts: origins, definitions, and functions in health and disease, Cell 184 (15) (2021 Jul 22) 3852–3872, https://doi.org/10.1016/j.cell.2021.06.024 (PMID: 34297930; PMCID: PMC8566693).
[4] F. Boraldi, F.D. Lofaro, S. Bonacorsi, A. Mazzilli, M. Garcia-Fernandez, D. Quaglino, The role of fibroblasts in skin homeostasis and repair, Biomedicines 12 (7) (2024 Jul 17) 1586, https://doi.org/10.3390/biomedicines12071586 (PMID: 39062158; PMCID: PMC1184439).
[5] A. Stunova, L. Vistejnova, Dermal fibroblasts-a heterogeneous population with regulatory function in wound healing, Cytokine Growth Factor Rev. 39 (2018 Feb) 137–150, https://doi.org/10.1016/j.cytogfr.2018.01.003 (Epub 2018 Feb 1. PMID: 29395658).
[6] M.L. Liu, T. Zang, Y. Zou, J.C. Chang, J.R. Gibson, K.M. Huber, C.L. Zhang, Small molecules enable neurogenin 2 to efficiently convert human fibroblasts into cholinergic neurons, Nat. Commun. 4 (2013) 2183, https://doi.org/10.1038/ncomms3183 (PMID: 23873306; PMCID: PMC3843951).
[7] M. Vangipuram, D. Ting, S. Kim, R. Diaz, B. Schüle, Skin punch biopsy explant culture for derivation of primary human fibroblasts, J. Vis. Exp. 77 (2013, Jul 7) e3779, https://doi.org/10.3791/3779 (PMID: 23852182; PMCID: PMC3731437).
[8] J. Ladewig, J. Mertens, J. Kesavan, J. Doerr, D. Poppe, F. Glaue, S. Herms, P. Wernet, G. Kögler, F.J. Müller, P. Koch, O. Brüstle, Small molecules enable highly efficient neuronal conversion of human fibroblasts, Nat. Methods 9 (6) (2012 Jun) 575–578, https://doi.org/10.1038/nmeth.1972 (Epub 2012 Apr 8. PMID: 22484851).
[9] E. Momotyuk, N. Ebrahim, K. Shakirova, E. Dashinimaev, Role of the cytoskeleton in cellular reprogramming: effects of biophysical and biochemical factors, Front. Mol. Biosci. Mar 7 (12) (2025) 1538806, https://doi.org/10.3389/fmolb.2025.1538806 (PMID: 40123979; PMCID: PMC11926148).
[10] K. Lee, Y.Y. Jo, G. Chung, J.H. Jung, Y.H. Kim, C.K. Park, Functional importance of transient receptor potential (TRP) channels in neurological disorders, Front. Cell Dev. Biol. Mar 4 (9) (2021) 611773, https://doi.org/10.3389/fcell.2021.611773 (PMID: 33748103; PMCID: PMC7969799).
[11] M.J. Caterina, Z. Pang, TRP channels in skin biology and pathophysiology, Pharmaceuticals (Basel) 9 (4) (2016 Dec 14) 77, https://doi.org/10.3390/ph9040077 (PMID: 27983625; PMCID: PMC5198052).
[12] Y. Xia, L. Xia, L. Lou, R. Jin, H. Shen, W. Li, Transient receptor potential channels and chronic airway inflammatory diseases: a comprehensive review, Lung 196 (5) (2018 Oct) 505–516, https://doi.org/10.1007/s00408-018-0145-3 (Epub 2018 Aug 9. PMID: 30094794).
[13] Y. Yang, R. Chen, X. Wu, Y. Zhao, Y. Fan, Z. Xiao, J. Han, L. Sun, X. Wang, J. Dai, Rapid and efficient conversion of human fibroblasts into functional neurons by small molecules, Stem Cell Rep. 13 (5) (2019 Nov 12) 862–876, https://doi.org/10.1016/j.stemcr.2019.09.007 (Epub 2019 Oct 17. PMID: 31631018; PMCID: PMC6893066).
[14] Y. Xue, K. Ouyang, J. Huang, Y. Zhou, H. Ouyang, H. Li, G. Wang, Q. Wu, C. Wei, Y. Bi, L. Jiang, Z. Cai, H. Sun, K. Zhang, Y. Zhang, J. Chen, X.D. Fu, Direct conversion of fibroblasts to neurons by reprogramming PTB-regulated microRNA circuits, Cell 152 (1–2) (2013 Jan 17) 82–96, https://doi.org/10.1016/j.cell.2012.11.045 (Epub 2013 Jan 11. PMID: 23313552; PMCID: PMC3552026).
[15] A.I. Abdullah, A. Pollock, T. Sun, The path from skin to brain: generation of functional neurons from fibroblasts, Mol. Neurobiol. 45 (3) (2012 Jun) 586–595, https://doi.org/10.1007/s12035-012-8277-6 (Epub 2012 May 22. PMID: 22614130; PMCID: PMC3564239).
[16] K. Kulangara, A.F. Adler, H. Wang, M. Chellappan, E. Hammett, R. Yasuda, K. W. Leong, The effect of substrate topography on direct reprogramming of fibroblasts to induced neurons, Biomaterials 35 (20) (2014 Jul) 5327–5336, https://doi.org/10.1016/j.biomaterials.2014.03.034.
[17] T.L. Downing, J. Soto, C. Morez, T. Houssin, A. Fritz, F. Yuan, J. Chu, S. Patel, D. V. Schaffer, S. Li, Biophysical regulation of epigenetic state and cell reprogramming, Nat. Mater. 12 (12) (2013 Dec) 1154–1162, https://doi.org/10.1038/nmat3777 (Epub 2013 Oct 20. PMID: 24141451; PMCID: PMC9675045).
[18] J. Yoo, M. Noh, H. Kim, N.L. Jeon, B.S. Kim, J. Kim, Nanogrooved substrate promotes direct lineage reprogramming of fibroblasts to functional induced dopaminergic neurons, Biomaterials 45 (2015, Mar) 36–45, https://doi.org/10.1016/j.biomaterials.2014.12.049 (Epub 2015 Jan 13. PMID: 25662493).
[18a] E. Kang, G. Jeong, Y. Choi, et al., Digitally tunable physicochemical coding of material composition and topography in continuous microfibres, Nature Mater. 10 (2011) 877–883, https://doi.org/10.1038/nmat3108.
[18b] Y. Hu, Z. Chen, H. Wang, J. Guo, J. Cai, X. Chen, H. Wei, J. Qi, Q. Wang, H. Liu, Y. Zhao, R. Chai, Conductive nerve guidance conduits based on morpho butterfly wings for peripheral nerve repair, ACS Nano 16 (2) (2022) 1868–1879, https://doi.org/10.1021/acsnano.1c11627.
[18c] H. Wei, Z.Y. Chen, Y.N. Hu, W. Cao, X.F. Ma, C. Zhang, X. Gao, X.Y. Qian, Y. J. Zhao, R.J. Chai, Topographically conductive butterfly wing substrates for directed spiral ganglion neuron growth, Small 17 (2021) 2102062, https://doi.org/10.1002/smll.202102062.

[19] L. Fernández-García, J. Pérez-Rigueiro, R. Martinez-Murillo, F. Panetsos, M. Ramos, G.V. Guinea, D. González-Nieto, Cortical reshaping and functional recovery induced by silk fibroin hydrogels-encapsulated stem cells implanted in stroke animals, Front. Cell. Neurosci. 6 (12) (2018 Sep) 296, https://doi.org/10.3389/fncel.2018.00296 (PMID: 30237762; PMCID: PMC6135908).
[20] Z. Chen, H. Bi, X. Ding, Topographical cues of biomaterials and fibroblast activation: are they related? Mechanobiol Med. 2 (1) (2023 Oct 31) 100028 https://doi.org/10.1016/j.mbm.2023.100028 (PMID: 40458549; PMCID: PMC12128637).
[21] J. Zhu, Y. Du, L.J. Backman, J. Chen, H. Ouyang, W. Zhang, Cellular interactions and biological effects of silk fibroin: implications for tissue engineering and regenerative medicine, Small 21 (4) (2025 Jan) e2409739, https://doi.org/10.1002/smll.202409739 (Epub 2024 Dec 12. PMID: 39668424).
[22] A.M. Moysenovich, V.V. Tatarskiy, M.A. Yastrebova, I.V. Bessonov, A. Y. Arkhipova, A.S. Kolosov, L.I. Davydova, A.I. Khamidullina, V.G. Bogush, V. G. Debabov, K.V. Shaitan, A.A. Shtil, M.M. Moisenovich, Akt and Src mediate the photocrosslinked fibroin-induced neural differentiation, Neuroreport 31 (10) (2020 Jul 10) 770–775, https://doi.org/10.1097/WNR.0000000000001482 (PMID: 32467514; PMCID: PMC7289124).
[23] A. Sagnella, A. Pistone, S. Bonetti, A. Donnadio, E. Saracino, M. Nocchetti, C. Dionigi, G. Ruani, M. Muccini, T. Posati, V. Benfenati, R. Zamboni, Effect of different fabrication methods on the chemo-physical properties of silk fibroin films and on their interaction with neural cells, RSC Adv. 6 (2016) 9304–9314, https://doi.org/10.1039/C5RA20684G.
[24] A. Pistone, A. Sagnella, C. Chieco, G. Bertazza, G. Varchi, F. Formaggio, T. Posati, E. Saracino, M. Caprini, S. Bonetti, S. Toffanin, N. Di Virgilio, M. Muccini, F. Rossi, G. Ruani, R. Zamboni, V. Benfenati, Silk fibroin film from golden-yellow Bombyx mori is a biocomposite that contains lutein and promotes axonal growth of primary neurons, Biopolymers 105 (5) (2016 May) 287–299, https://doi.org/10.1002/bip.22806.
[25] V. Benfenati, S. Toffanin, C. Chieco, A. Sagnella, N. Di Virgilio, T. Posati, G. Varchi, M. Natali, G. Ruani, M. Muccini, F. Rossi, R. Zamboni, Silk fibroin based technology for industrial biomanufacturing, in: Factories of the Future, Springer International Publishing, Cham, 2019, pp. 409–430. First Online: 15 February 2019, https://doi.org/10.1007/978-3-319-94358-9_19.
[26] V. Benfenati, S. Toffanin, R. Capelli, L.M. Camassa, S. Ferroni, D.L. Kaplan, F. G. Omenetto, M. Muccini, R. Zamboni, A silk platform that enables electrophysiology and targeted drug delivery in brain astroglial cells, Biomaterials 31 (31) (2010 Nov) 7883–7891, https://doi.org/10.1016/j.biomaterials.2010.07.013 (Epub 2010 Aug 4. PMID: 20688390; PMCID: PMC2966966).
[27] V. Benfenati, A. Pistone, A. Sagnella, K. Stahl, L. Camassa, C. Gomis-Perez, S. Toffanin, R. Torp, D.L. Kaplan, G. Ruani, F.G. Omenetto, R. Zamboni, M. Muccini, WITHDRAWN: silk fibroin films are a bio-active interface for neuroregenerative medicine, J. Appl. Biomater. Funct. Mater. 20 (2012 Dec) 315–323, https://doi.org/10.5301/JABFM.2012.10448 (Epub ahead of print. PMID: 23258563).
[28] T. Posati, A. Pistone, E. Saracino, F. Formaggio, M.G. Mola, E. Troni, A. Sagnella, M. Nocchetti, M. Barbalinardo, F. Valle, S. Bonetti, M. Caprini, G.P. Nicchia, R. Zamboni, M. Muccini, V. Benfenati, A nanoscale Interface promoting molecular and functional differentiation of neural cells, Sci. Rep. 9 (6) (2016 Aug) 31226, https://doi.org/10.1038/srep31226 (PMID: 27503424; PMCID: PMC4977496).
[29] P. Anantha, P. Raj, E. Saracino, J.H. Kim, J.H. Kim, A. Convertino, L. Gu, I. Barman, Uncovering astrocyte morphological dynamics using optical diffraction tomography and shape-based trajectory inference, Adv. Healthc. Mater. 14 (6) (2025 Mar) e2402960, https://doi.org/10.1002/adhm.202402960. Epub 2024 Dec 30, 39740118.
[30] T. O'Connor, A. Anand, B. Andemariam, B. Javidi, Deep learning-based cell identification and disease diagnosis using spatio-temporal cellular dynamics in compact digital holographic microscopy, Biomed. Opt. Express. 11 (8) (2020 Jul 21) 4491–4508, https://doi.org/10.1364/BOE.399020 (PMID: 32923059; PMCID: PMC7449709).
[31] X. Yu, J. Hong, C. Liu, M.K. Kim, Review of digital holographic microscopy for three-dimensional profiling and tracking, Opt. Eng. 53 (11) (2014) 112306, https://doi.org/10.1117/1.OE.53.11.112306.
[32] B. Kemper, A. Bauwens, D. Bettenworth, M. Götte, B. Greve, L. Kastl, S. Ketelhut, P. Lenz, S. Mues, J. Schnekenburger, A. Vollmer, Label-free quantitative in vitro live cell imaging with digital holographic microscopy, in: Bioanalytical Reviews vol 2, Springer Berlin Heidelberg, Berlin, Heidelberg, 2019, https://doi.org/10.1007/11663_2019_6.
[33] W. Choi, C. Fang-Yen, K. Badizadegan, S. Oh, N. Lue, R.R. Dasari, M.S. Feld, Tomographic phase microscopy, Nat. Methods 4 (9) (2007 Sep) 717–719, https://doi.org/10.1038/nmeth1078 (Epub 2007 Aug 12. PMID: 17694065).
[34] P. Anantha, Z. Liu, P. Raj, I. Barman, Optical diffraction tomography and Raman spectroscopy reveal distinct cellular phenotypes during white and brown adipocyte differentiation, Biosens. Bioelectron. 235 (2023 Sep 1) 115388, https://doi.org/10.1016/j.bios.2023.115388 (Epub 2023 May 12. PMID: 37207582; PMCID: PMC10626559).
[35] Z. Liu, S. Parida, S. Wu, C.L. Sears, D. Sharma, I. Barman, Label-free vibrational and quantitative phase microscopy reveals remarkable pathogen-induced morphomolecular divergence in tumor-derived cells, ACS Sens. 7 (5) (2022 May 27) 1495–1505, https://doi.org/10.1021/acssensors.2c00232 (Epub 2022 May 18. PMID: 35583030).
[36] P. Anantha, X. Wu, S. Elsaid, P. Raj, J. Hu, I. Barman, S.S. Tee, Sweet science: exploring the impact of fructose and glucose on brown adipocyte differentiation using optical diffraction tomography, J. Cell. Biochem. 126 (6) (2025 Jun) e70052, https://doi.org/10.1002/jcb.70052 (PMID: 40583297; PMCID: PMC12207058).
[37] G. Popescu, Y. Park, Quantitative phase imaging in biomedicine, J. Biomed. Opt. 20 (11) (2015 Nov) 111201, https://doi.org/10.1117/1.JBO.20.11.111201 (PMID: 26648557).
[38] K. Lee, K. Kim, J. Jung, J. Heo, S. Cho, S. Lee, G. Chang, Y. Jo, H. Park, Y. Park, Quantitative phase imaging techniques for the study of cell pathophysiology: from principles to applications, Sensors (Basel). 13 (4) (2013 Mar 28) 4170–4191, https://doi.org/10.3390/s130404170 (PMID: 23539026; PMCID: PMC3673078).
[39] P. Anantha, A. Gupta, J.H. Kim, E. Saracino, P. Raj, I. Lucarini, S. Tanwar, J. Chen, L. Gu, J. Agrawal, A. Convertino, I. Barman, Disordered glass nanowire substrates produce in vivo-like astrocyte morphology revealed by low-coherence holotomography, Adv Sci (Weinh). 3 (2025 Nov) e13424, https://doi.org/10.1002/advs.202513424 (Epub ahead of print. PMID: 41178585).
[40] B.D. Lawrence, F. Omenetto, K. Chui, D.L. Kaplan, Processing methods to control silk fibroin film biomaterial features, J. Mater. Sci. 43 (21) (2008) 6967–6985, https://doi.org/10.1007/s10853-008-2895-3.
[41] M. Barbalinardo, M. Giannelli, L. Forcini, B. Luppi, A. Donnadio, M.L. Navacchia, G. Ruani, G. Sotgiu, A. Aluigi, R. Zamboni, T. Posati, Eco-sustainable silk fibroin/pomegranate peel extract film as an innovative green material for skin repair, Int. J. Mol. Sci. 23 (12) (2022) 6805, https://doi.org/10.3390/ijms23126805.
[42] V. Benfenati, K. Stahl, C. Gomis-Perez, S. Toffanin, A. Sagnella, R. Torp, D. L. Kaplan, F.G. Omenetto, G. Ruani, M. Muccini, G. Lanzani, K. Kostarelos, D. Scaini, L. Ballerini, R. Zamboni, Biofunctional silk/neuron interfaces, Adv. Funct. Mater. 22 (9) (2012) 1871–1884, https://doi.org/10.1002/adfm.201102310.
[43] C. Allier, L. Hervé, O. Mandula, P. Blandin, Y. Usson, J. Savatier, S. Monneret, S. Morales, Quantitative phase imaging of adherent mammalian cells: a comparative study, Biomed Opt Express. 10 (6) (2019 May 14) 2768–2783, https://doi.org/10.1364/BOE.10.002768 (PMID: 31259050; PMCID: PMC6583341).
[44] S.K. Paidi, P. Raj, R. Bordett, C. Zhang, S.H. Karandikar, R. Pandey, I. Barman, Raman and quantitative phase imaging allow morpho-molecular recognition of malignancy and stages of B-cell acute lymphoblastic leukemia, Biosens. Bioelectron. 15 (190) (2021 Oct) 113403, https://doi.org/10.1016/j.bios.2021.113403 (Epub 2021 Jun 12. PMID: 34130086; PMCID: PMC8492164).
[45] W. Choi, C. Fang-Yen, K. Badizadegan, S. Oh, N. Lue, R.R. Dasari, M.S. Feld, Tomographic phase microscopy, Nat. Methods 4 (9) (2007 Sep) 717–719, https://doi.org/10.1038/nmeth1078 (Epub 2007 Aug 12. PMID: 17694065).
[46] Z. Liu, S. Parida, S. Wu, C.L. Sears, D. Sharma, I. Barman, Label-free vibrational and quantitative phase microscopy reveals remarkable pathogen-induced morphomolecular divergence in tumor-derived cells, ACS Sens. 7 (5) (2022 May 27) 1495–1505, https://doi.org/10.1021/acssensors.2c00232 (Epub 2022 May 18. PMID: 35583030).
[47] P. Raj, S.K. Paidi, L. Conway, A. Chatterjee, I. Barman, CellSNAP: a fast, accurate algorithm for 3D cell segmentation in quantitative phase imaging, J. Biomed. Opt. 29 (Suppl 2) (2024 Jun) S22706, https://doi.org/10.1117/1.JBO.29.S2.S22706 (Epub 2024 Apr 18. PMID: 38638450; PMCID: PMC11025678).
[48] H. Rubin, Cell aging in vivo and in vitro, Mech. Ageing Dev. 98 (1) (1997 Oct) 1–35, https://doi.org/10.1016/s0047-6374(97)00067-5 (PMID: 9255755).
[49] L. Ottaviano, S. Buoso, R. Zamboni, G. Sotgiu, T. Posati, Natural protein films from textile waste for wound healing and wound dressing applications, J. Funct. Biomater. 16 (1) (2025) 20, https://doi.org/10.3390/jfb16010020.
[50] W. Sun, T. Incitti, C. Migliaresi, A. Quattrone, S. Casarosa, A. Motta, Viability and neuronal differentiation of neural stem cells encapsulated in silk fibroin hydrogel functionalized with an IKVAV peptide, J. Tissue Eng. Regen. Med. 11 (5) (2017 May) 1532–1541, https://doi.org/10.1002/term.2053 (Epub 2015 Jun 5. PMID: 26053955).
[51] M.D. Tang-Schomer, D.L. Kaplan, M.J. Whalen, Film interface for drug testing for delivery to cells in culture and in the brain, Acta Biomater. 94 (2019 Aug) 306–319, https://doi.org/10.1016/j.actbio.2019.02.052 (Epub 2019 Mar 2. PMID: 30836199; PMCID: PMC6642835).
[52] L. Yang, S. Pijuan-Galito, H.S. Rho, A.S. Vasilevich, A.D. Eren, L. Ge, P. Habibović, M.R. Alexander, J. de Boer, A. Carlier, P. van Rijn, Q. Zhou, High-throughput methods in the discovery and study of biomaterials and materiobiology, Chem. Rev. 121 (8) (2021 Apr 28) 4561–4677, https://doi.org/10.1021/acs.chemrev.0c00752 (Epub 2021 Mar 11. PMID: 33705116; PMCID: PMC8154331).
[53] D. Naskar, S. Nayak, T. Dey, S.C. Kundu, Non-mulberry silk fibroin influence osteogenesis and osteoblast-macrophage cross talk on titanium based surface, Sci. Rep. 22 (4) (2014 Apr) 4745, https://doi.org/10.1038/srep04745 (PMID: 24752225; PMCID: PMC3994497).
[54] A.J. Engler, S. Sen, H.L. Sweeney, D.E. Discher, Matrix elasticity directs stem cell lineage specification, Cell 126 (4) (2006 Aug 25) 677–689, https://doi.org/10.1016/j.cell.2006.06.044 (PMID: 16923388).
[55] S. Dupont, L. Morsut, M. Aragona, E. Enzo, S. Giulitti, M. Cordenonsi, F. Zanconato, J. Le Digabel, M. Forcato, S. Bicciato, N. Elvassore, S. Piccolo, Role of YAP/TAZ in mechanotransduction, Nature 474 (7350) (2011 Jun 8) 179–183, https://doi.org/10.1038/nature10137 (PMID: 21654799).
[56] D. Chester, V. Lee, P. Wagner, M. Nordberg, M.B. Fisher, A.C. Brown, Elucidating the combinatorial effect of substrate stiffness and surface viscoelasticity on cellular phenotype, J. Biomed. Mater. Res. A 110 (6) (2022 Jun) 1224–1237, https://doi.org/10.1002/jbm.a.37367 (Epub 2022 Feb 1. PMID: 35107204; PMCID: PMC9305170).
[57] M. Sousa de Almeida, A. Lee, F. Itel, K. Maniura-Weber, A. Petri-Fink, B. Rothen-Rutishauser, The effect of substrate properties on cellular behavior and nanoparticle uptake in human fibroblasts and epithelial cells, Nanomaterials

(Basel) 14 (4) (2024 Feb 10) 342, https://doi.org/10.3390/nano14040342 (PMID: 38392715; PMCID: PMC10892529).
[58] K. Xie, Y. Yang, H. Jiang, Controlling cellular volume via mechanical and physical properties of substrate, Biophys J. 114 (3) (2018 Feb 6) 675–687, https://doi.org/10.1016/j.bpj.2017.11.3785 (PMID: 29414713; PMCID: PMC5985025).
[59] E. Passeri, A.M. Wilson, A. Primerano, M.A. Kondo, S. Sengupta, R. Srivastava, M. Koga, C. Obie, P.P. Zandi, F.S. Goes, D. Valle, J.L. Rapoport, A. Sawa, S. Kano, K. Ishizuka, Enhanced conversion of induced neuronal cells (iN cells) from human fibroblasts: utility in uncovering cellular deficits in mental illness-associated chromosomal abnormalities, Neurosci. Res. 101 (2015 Dec) 57–61, https://doi.org/10.1016/j.neures.2015.07.011 (Epub 2015 Aug 7. PMID: 26260244; PMCID: PMC4774521.013).